

JUL 22 1988

**AEDC-TR-87-39**

C.3



## **Analysis of Edge Detection Techniques for Radiographic Image Measurement**

**A. L. Nasser**  
Sverdrup Technology, Inc.

**April 1988**

**PROPERTY OF U.S. AIR FORCE  
AEDC TECHNICAL LIBRARY**

**Final Report for Period January 1986 — November 1987**

**TECHNICAL REPORTS  
FILE COPY**

Approved for public release; distribution is unlimited.

**ARNOLD ENGINEERING DEVELOPMENT CENTER  
ARNOLD AIR FORCE BASE, TENNESSEE  
AIR FORCE SYSTEMS COMMAND  
UNITED STATES AIR FORCE**

## NOTICES

When U. S. Government drawings, specifications, or other data are used for any purpose other than a definitely related Government procurement operation, the Government thereby incurs no responsibility nor any obligation whatsoever, and the fact that the Government may have formulated, furnished, or in any way supplied the said drawings, specifications, or other data, is not to be regarded by implication or otherwise, or in any manner licensing the holder or any other person or corporation, or conveying any rights or permission to manufacture, use, or sell any patented invention that may in any way be related thereto.

Qualified users may obtain copies of this report from the Defense Technical Information Center.

References to named commercial products in this report are not to be considered in any sense as an endorsement of the product by the United States Air Force or the Government.

This report has been reviewed by the Office of Public Affairs (PA) and is releasable to the National Technical Information Service (NTIS). At NTIS, it will be available to the general public, including foreign nations.

## APPROVAL STATEMENT

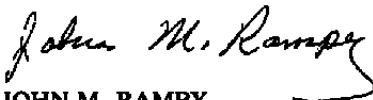
This report has been reviewed and approved.



THEODORE A. BAPTY, 1st Lt, USAF  
Directorate of Technology  
Deputy for Operations

Approved for publication:

FOR THE COMMANDER



JOHN M. RAMPY  
Directorate of Technology  
Deputy for Operations

UNCLASSIFIED

SECURITY CLASSIFICATION OF THIS PAGE

REPORT DOCUMENTATION PAGE				Form Approved OMB No. 0704-0188	
1a. REPORT SECURITY CLASSIFICATION Unclassified			1b. RESTRICTIVE MARKINGS		
2a. SECURITY CLASSIFICATION AUTHORITY			3. DISTRIBUTION/AVAILABILITY OF REPORT Approved for public release; distribution is unlimited.		
2b. DECLASSIFICATION/DOWNGRADING SCHEDULE					
4. PERFORMING ORGANIZATION REPORT NUMBER(S) AEDC-TR-87-39			5. MONITORING ORGANIZATION REPORT NUMBER(S)		
6a. NAME OF PERFORMING ORGANIZATION Arnold Engineering Development Center		6b. OFFICE SYMBOL (if applicable) DOP	7a. NAME OF MONITORING ORGANIZATION		
6c. ADDRESS (City, State, and ZIP Code) Air Force Systems Command Arnold Air Force Base, TN 37389-5000			7b. ADDRESS (City, State, and ZIP Code)		
8a. NAME OF FUNDING/SPONSORING ORGANIZATION Arnold Engineering Development Center		8b. OFFICE SYMBOL (if applicable) DOT	9. PROCUREMENT INSTRUMENT IDENTIFICATION NUMBER		
8c. ADDRESS (City, State, and ZIP Code) Air Force Systems Command Arnold Air Force Base, TN 37398-5000			10. SOURCE OF FUNDING NUMBERS		
			PROGRAM ELEMENT NO 65807F	PROJECT NO DB90EW	TASK NO
			WORK UNIT ACCESSION NO		
11. TITLE (Include Security Classification) Analysis of Edge Detection Techniques for Radiographic Image Measurement (U)					
12. PERSONAL AUTHOR(S) Nasser, A.L., Sverdrup Technology, Inc., AEDC Group					
13a. TYPE OF REPORT Final		13b. TIME COVERED FROM 1/86 to 11/87		14. DATE OF REPORT (Year, Month, Day) April 1988	
15. PAGE COUNT 41					
16. SUPPLEMENTARY NOTATION Available in Defense Technical Information Center (DTIC).					
17. COSATI CODES			18. SUBJECT TERMS (Continue on reverse if necessary and identify by block number)		
FIELD	GROUP	SUB-GROUP			
14	05		image analysis solid rocket motors		
			radiography nozzle erosion		
			edge detection		
19. ABSTRACT (Continue on reverse if necessary and identify by block number)					
<p>Personnel at the Arnold Engineering Development Center (AEDC) routinely X-ray inspect solid rocket motors. From the visual inspection of these data, potentially dangerous situations have been avoided by preventing the test of damaged rocket motors. However, an objective like rocket nozzle erosion cannot be analyzed in a timely fashion because of the detailed inspection required per frame of videotape, and the number of frames for a typical rocket motor firing.</p> <p>The goal of this study was to evaluate computer image measurement techniques so a process like measurement of rocket motor nozzle throat erosion can be automated for timely analysis. After evaluation of several edge detection techniques, two procedures were found to be satisfactory for this task. This study has determined that radiographic images can be measured accurately to within 0.14 inches by timely computer analysis.</p>					
20. DISTRIBUTION/AVAILABILITY OF ABSTRACT <input type="checkbox"/> UNCLASSIFIED/UNLIMITED <input checked="" type="checkbox"/> SAME AS RPT. <input type="checkbox"/> DTIC USERS			21. ABSTRACT SECURITY CLASSIFICATION Unclassified		
22a. NAME OF RESPONSIBLE INDIVIDUAL C.L. Garner			22b. TELEPHONE (Include Area Code) (615) 454-7813		22c. OFFICE SYMBOL DOCS

## **PREFACE**

The work reported herein was conducted by the Arnold Engineering Development Center (AEDC), Air Force Systems Command (AFSC) from January 1986 to November 1987 under Program Element 65807F, Project No. DB90EW, at the request of the AEDC Directorate of Technology. The results were obtained by Sverdrup Technology, Inc., AEDC Group, operating contractor for the propulsion test effort at the Arnold Engineering Development Center, AFSC, Arnold Air Force Base, Tennessee. The manuscript was submitted for publication on January 15, 1988.

## CONTENTS

	<u>Page</u>
1.0 INTRODUCTION .....	5
2.0 DETECTION TECHNIQUES .....	5
3.0 EDGE DETECTION EXPERIMENTS .....	9
3.1 Rocket Nozzle Throat Simulator .....	9
3.2 Setup for Data Acquisition .....	9
3.3 Experimental Results .....	10
4.0 CONCLUSIONS .....	12
5.0 REFERENCES .....	13

## ILLUSTRATIONS

<u>Figure</u>	<u>Page</u>
1. An Example of Averaging and Thresholding .....	15
2. Use of the Threshold Method .....	16
3. Different Techniques for Approximating the Gradient of an Image .....	17
4. Use of the K-Means Algorithm .....	18
5. Typical Profile for Performance Index .....	20
6. Overview of Nozzle Throat Simulator .....	21
7. Details of Simulated Throat Sections .....	22
8. Computer Image of Simulator .....	23
9. Object Magnified by 100 percent .....	24
10. Data Acquisition for Setup No. 2 .....	25
11. Example of an Image Area Selection .....	26
12. Application of Laplacian Operator .....	28
13. Variance in Plate-to-Plate Graylevel Intensity .....	29
14. Throat Simulator Image Histogram .....	30
15. Application of Prewitt Operator .....	31
16. Application of Sobel Operator .....	32
17. Problem with Graylevel Thresholding .....	33
18. Influence of Area Selection of K-Means Results .....	34

**TABLES**

<b><u>Table</u></b>	<b><u>Page</u></b>
1. Edge Detection Results on a Good Image .....	35
2. Edge Detection Results for Various Test Setups .....	36
3. Computer versus Visual Results .....	37

## 1.0 INTRODUCTION

Personnel at the Arnold Engineering Development Center routinely use X-ray radiography to inspect solid-propellant rocket motors. From the visual inspection of these data, potentially dangerous situations have been avoided by preventing the test of damaged rocket motors. However, radiography could also be used to determine rocket nozzle throat erosion (due to the high temperatures and dynamics of combustion, a rocket nozzle throat can become larger and affect thrust and specific impulse), provided that a method for timely X-ray analysis can be found.

In 1985, a Quantex real-time digital image processor was purchased. With this device, X-ray data recorded on videotape (real-time radiography, RTR) could be analyzed moments after acquisition and could be used to highlight objects of interest within the motor case (for example, the nozzle throat) by frame averaging, filtering, and contrast stretching. Still, measuring rocket nozzle throat erosion during a test could not be accurately analyzed in a timely fashion because of the detailed inspection required per frame of videotape and the number of frames for a typical rocket motor firing. Therefore, this type of analysis could not be efficiently and accurately performed unless the process was automated by computer.

The purpose of this study was to evaluate possible edge detection techniques that could be used to automate X-ray image analysis, providing more accurate and expedient results than from measurement by visual inspection.

In Section 2.0 an overview of candidate edge detection procedures is presented, and the effectiveness of several detection techniques is presented in Section 3.0. Finally, conclusions and recommendations are presented in the final section of this report.

## 2.0 DETECTION TECHNIQUES

An object within an image will be observed as an intensity discontinuity. For example, in an image of the moon and surrounding sky, the moon will appear light and the sky as dark. As a row of image pixel intensities is scanned, the moon's edge will be located when a transformation from dark to light (or vice versa) intensity is noted. Gonzalez and Wintz (Ref. 1) call this the "Gray-Level Thresholding" technique for edge detection.

In the example just illustrated, a gray-level (image pixel intensity) threshold value is established, and once this threshold value is exceeded, the edge is established. In most instances, the threshold value will be determined based upon prior knowledge about the principal brightness regions or a percentage increase in intensity (Ref. 1).

Davis, Rosenfeld, and Weszka (Ref. 2) illustrate the example of thresholding with local pixel intensity averaging as shown in Fig. 1. Initially, image noise was reduced by local averaging. The object can then be identified from the region by setting a gray-level threshold value (in this case, the threshold was set at 32 on a scale of 0 for black to 63 for white), and requiring that everything below gray level 32 be part of the object. Figure 2 shows how a selected threshold can determine image object from background. In this figure, pixels with an intensity above 32 were selected as the object (the highlighted column of image data was plotted versus vertical pixel image location).

The most common and historically earliest edge operator is the gradient (Ref. 3). Given a function  $f(x,y)$ , the gradient of  $f$  at coordinates  $(x,y)$  is defined as the vector:

$$G[F(x,y)] = \begin{bmatrix} \frac{\partial f}{\partial x} \\ \frac{\partial f}{\partial y} \end{bmatrix} \quad (1)$$

Gonzalez and Wintz (Ref. 1) indicate two important properties of the gradient,  $G[f(x,y)]$ :

1. The vector  $G[f(x,y)]$  points in the direction of the maximum rate of change of the function  $f(x,y)$ .
2. The magnitude of  $G[f(x,y)]$  equals the maximum rate of change of  $f(x,y)$  per unit distance in the direction of  $G$ , as given by:

$$\text{mag}[G] = \left[ \left( \frac{\partial f}{\partial x} \right)^2 + \left( \frac{\partial f}{\partial y} \right)^2 \right]^{1/2} \quad (2)$$

For a digital image, the derivatives for the magnitude of  $[G]$  are used to detect image edges, and these are approximated by spatial differences. One technique for approximating the gradient magnitude is called the Roberts (Ref. 1) gradient, and is defined by:

$$G[f(x,y)] = \left[ [f(x,y) - f(x+1, y+1)] + [f(x+1,y) - f(x,y+1)] \right] \quad (3)$$

The Roberts mask is shown graphically in Fig. 3a. Given an image  $f(x,y)$ , the  $m \times n$  mask produces the gradient image  $G(x,y)$  by:

$$G(x,y) = \sum_s f(n,m) \quad (4)$$



where  $S$  is the set of all points in the mask. Figures 3b and 3c present the masks of two other gradient approximations (that of Prewitt and Sobel, Ref. 3). These other masks use more pixels in approximation of the gradient magnitude ( $f(x,y)$  is the center), and the Sobel procedure weights some pixels more heavily than others (the pixels located closer to  $f(x,y)$  are weighted more heavily). In fact, these modified operators (Prewitt and Sobel) tend to reduce the effects of noise (Ref. 3) and are found to be more useful in practical image analysis situations.

The Laplacian of a two-variable function  $f(x,y)$  is defined as:

$$\nabla^2 f(x,y) = \frac{\partial^2 f}{\partial x^2} + \frac{\partial^2 f}{\partial y^2} \quad (5)$$

One version (Ref. 3) of the discrete Laplacian,  $L(x,y)$ , is:

$$L(x,y) = f(x,y) - 1/4*[f(x,y+1) + f(x,y-1) + f(x+1,y) + f(x-1,y)] \quad (6)$$

The discrete Laplacian has been used as edge detector much like the discrete gradient. However, the discrete Laplacian has fallen into disfavor for edge detection because, as it is an approximation to the second derivatives, noise in the image can become more enhanced than the image object itself (Ref. 3).

Another technique for edge detection is pixel clustering as described by Tou and Gonzalez (Ref. 4). Image pixels are clustered into groups by specific characteristics (that is, location and gray-level intensity) and the image edges will be those pixels bordering the different groups (clusters). In general, the clustering criterion used will be based on the minimization (or maximization) of a certain performance index. One of the most often used indices is the sum of the squared errors index (used in the K-means concept to be described), which is defined as:

$$J = \sum_{j=1}^{N_c} \sum_{x \in S_j} \|x - m_j\|^2 \quad (7)$$

where  $N_c$  is the number of cluster domains,  $S_j$  is the set of samples belonging to the  $j$ th domain, and

$$m_j = \frac{1}{N_j} \sum_{x \in S_j} x \quad (8)$$

where  $N_j$  represents the number of samples in  $S_j$ .

The K-means algorithm (Ref. 4) is a specific clustering technique used to divide an image into cluster groups as just described. The K-means concept used in this effort can be summarized as follows:

Image data were averaged parallel to expected edge direction (to remove noise spikes without jeopardizing edge data; shown in Figs. 4a and b) and then arbitrarily divided into two clusters (A and B) as shown in Fig. 4c. A mean gray level value was calculated for each side, and the performance index was calculated by:

$$J = \sum_{j=1}^{N_c} \sum_{x \in S_j} \|x - z\|^2 \quad (9)$$

where  $z$  is the respective mean gray level value,  $x$  is the set of all pixels in each cluster, and  $N$  is the total number of clusters. Then one pixel is transferred from the B to A cluster and the performance index recalculated and the procedure is repeated until the performance index is minimized (Fig. 5).

The B cluster is defined to include most of the image points initially so the performance index will be a large number and decrease as the edge is approached. The expected trend in the performance index calculation as a function of the location of the line separating the clusters is shown in Fig. 5. The performance index will again increase toward its initial value when the edge is passed.

Pattern classification by likelihood functions were the final edge detectors to be examined, and these were also presented by Tou and Gonzalez (Ref. 4). The Bayes classifier is such an edge detector which assigns image points to region classifications based on a probability function. Each point in the image is systematically assigned a probability that it belongs to a certain region or class, and then the probability is adjusted until an optimal grouping (lowest probability of error) is found. Unfortunately, some *a priori* knowledge must be known about the image before probability assignments can be made; this is discussed in later sections of this report. Like the K-means clustering routine, the image edges will be those pixels bordering the class groupings.

In summary, the edge detectors investigated by this research were edge detection by thresholding, application of a gradient and Laplacian approximation, the K-means clustering technique, and the Bayes classifier. In the following sections, these techniques are compared using a single X-ray image, and the techniques providing the best detection results were compared on other images.

### 3.0 EDGE DETECTION EXPERIMENTS

#### 3.1 ROCKET NOZZLE THROAT SIMULATOR

The techniques presented in Sec. 2.0 were evaluated with a reference data set so that meaningful comparisons could be made. X-ray nozzle erosion data (a prime objective for automated image analysis) was selected as the focus of attention. Actual nozzle erosion data (from a live rocket firing) could not be used since the true erosion characteristics were either not available or accurately known. Therefore, a nozzle simulator was designed and constructed such that, when X-rayed, data would be provided for exactly known "throat" or hole diameters (Fig. 6).

The simulator was a 0.5-in.-thick plexiglass box containing a series of metal plates with varying diameter hole sizes. The box was approximately 24 in. long, and 15 in. in height and width. Solid lead or plexiglass plates could be added in front of or behind the varying throat sections to simulate a predetermined propellant loading (with the setup shown, the approximate simulated propellant loading was 11 in. from a 6-MeV source). Plate number 4 (with a 1.015-in. hole) was used as a pretest "known" measurement and plates 5 through 14 had progressively larger holes to simulate nozzle throat erosion during testing (to reflect an actual rocket test, the change between hole sizes decreased as relative hole size increased).

#### 3.2 SETUP FOR DATA ACQUISITION

The nozzle throat simulator was configured as shown in Fig. 7, and data were acquired (designated as setup 1A). A 6-MeV X-ray source provided 250 R at 1 meter from the source, and the source-to-object and source-to-camera distances were 12.7 and 14 ft, respectively. Then, an additional 1/4-in.-thick sheet of lead was added in front of and behind the simulated throat section to simulate a propellant loading of 15 in. The image displayed by this setup (1B) is shown in Fig. 8. The final configuration was a 2 x magnification of the second setup and is presented in Fig. 9. This was accomplished by decreasing the source-to-model distance to 7 ft (setup 1C). After image enhancement (by a four-frame moving average) and visual image inspection, more data were required because of the poor quality of the images generated (Fig. 8 and 9). Setups 2A and 2B are presented in Fig. 10. No propellant loading was simulated by these setups (no lead sheets were placed in front of or behind the simulated throat sections), and source-to-object and source-to-camera distances were the same as for setups 1A and 1C. These data were used to compare the different edge detector procedures as presented next.

### 3.3 EXPERIMENTAL RESULTS

Figure 11a shows how an image area containing an edge was selected for edge detection analysis. The image area consisted of  $n$  rows and  $m$  columns or  $n \times m$  total pixels. For all these analyses, the edge was parallel to the  $n$  direction as shown in the figure. These image data were averaged (to remove noise) along the  $m$  axis as shown in Fig. 11b. Since the edge was exactly in the  $n$  axis, no accuracy in detection was compromised because of noise reduction, and these data were input into the algorithms discussed earlier.

An example of the effectiveness of the discrete Laplacian as an edge detector is presented in Fig. 12. This figure shows that no specific edge can be located after application of the operator (ideally this operator should present a data spike at an edge location like the gradient example shown later). As discussed in Sec. 2.0, image noise can hamper edge detection by this technique; visual inspection of the image certainly confirmed that this image was not clear. Therefore, this technique was dismissed as a possible edge locator for this task.

The Bayes classifier cannot be easily applied to these data because the technique requires a statistical base in both the object and background surrounding areas for probability calculations. For example, if background pixel intensities ranged from 0 to 100, then everything above 100 would likely be an object pixel. However in this image, no such pattern was recognized. Figure 13 shows the difficulty in assigning a graylevel intensity probability to either area (object or background). Both object and background intensities vary across the image (likely attributable to nonuniformity of illumination). Figure 14 shows how some graylevel intensities for this image have the same probability of being object as they do of being background (this figure also shows the ideal image histogram for this edge detection technique). Therefore, this procedure was not included as a candidate image edge detector.

The gradient operator could be used as an edge detector for these data (this confirms previous experimentation by Walker, Gamble, and Smith, Ref. 5). The gradient approximations of Prewitt and Sobel were both tested and their effectiveness is shown in Figs. 15 and 16, respectively. Both operators indicate the same edge locations by the large data spikes at pixel locations 256 and 292, but the Sobel operator magnifies the intensity difference between the two edges (130 vs. 100). For this reason the Sobel operator was chosen for further study and was used to produce the results to be presented next.

Gradient edge detection results from throat simulator data (setup 2A) are presented in Table 1. These results show that the gradient operation will measure a 2.95-in. hole to within 12 percent (and the smaller holes more accurately). Although this error is greater than the expected pixel error (0.07 in. for a 1-in. image characterized by 39 pixels), the measurement yielded a consistently higher result than the true hole size by approximately 6 percent.

Edge detection by thresholding did not produce satisfactory results for these data (as shown for two hole sizes in Table 1). Figure 17 shows the graylevel intensity profile for the 1.7-in. hole. Because of the steep rise between pixel locations 214 and 254, the threshold calculation (1, 2, or 3 standard deviations) will indicate an edge well before the true edge pixel (No. 254). If this condition were true for all hole profiles (but it is not), the result would still yield a satisfactory answer (because the 1-in. reference measurement is located by the same procedure as the object to be measured, errors in edge location would cancel). To use this method, a relatively instantaneous increase or decrease must occur at or near the edge pixel (chance ramp intensity increases cause this method to yield unpredictable or erroneous results). Therefore, this method was dismissed for further research.

The K-means clustering technique did produce satisfactory edge detection results as shown in Table 1. These results indicated a measurement accuracy similar to that of the gradient; however, unlike the gradient operator, K-means results were influenced by the choice of image area selection. Figure 18 shows how two different image area selections will yield different results (pixel no. 219 might be selected as the edge for input of area no. 1 and no. 229 for input of area no. 2). Specifically, the 2.950-in. hole was measured to be 2.588 in. (12-percent error) and also 3.071 in. (4-percent error) by a different image area selection. Therefore, some standard for area selection had to be incorporated with this method as discussed in the following.

Since the gradient procedure cannot be influenced by operator image area selection, its results were used to dictate the image area to be input the K-means procedure to improve precision of measurement results. An equal number of pixels (nominally 15 - 20) on each side of the gradient result were input into the K-means routine, and the results obtained by incorporating the two methods are presented in Table 2. This table also shows the results obtained after image magnification (a 1-in. object in data set 2B was characterized by 68 pixels) and from degraded image analysis (added material through which the X-rays had to pass; setups 1A and 1C as presented in Sec. 3.2). In all cases but one, the results obtained from the combined procedures were more accurate than those from either method alone. In addition, justification has been established for the image area analyzed by the K-means procedure (the single instance shown where measurement by the K-means procedure alone produced a better measurement than the combined methods must be disregarded since no justification existed for image area selection, and another area could have just as easily been selected, producing opposite results). These results show that the largest error in measuring any of these objects was 0.14 in., regardless of image quality and/or magnification.

Table 3 presents measurement results obtained by visual inspection of plotted image data compared to those produced by the combined techniques just described. These results are approximately the same for both methods; however, it would be impossible to visually analyze

many frames of data in a timely fashion (subsequently, an automated method for the task has been established).

#### 4.0 CONCLUSIONS

The goal of this study was to evaluate computer image measurement techniques so that accurate measurement of rocket nozzle throat erosion could be automated for timely analysis. The results from this study are summarized as follows:

1. For these data, the Laplacian function, thresholding technique, and Bayes classifier could not be used to detect image edges.
2. The gradient function allowed image edges to be located without any operator interaction. The gradient produced excellent results for the good image data (reading consistently high, approximately 6 percent), but poor results on the degraded image (errors in measurement ranging from 11 to 21 percent).
3. The K-means algorithm produced satisfactory results if image area selection for analysis could be justified. The gradient function was used in combination with this method to justify data area selection, and the largest error in measurement for these experiments was 0.14 in., regardless of image quality and/or magnification.
4. Computer image measurement was not a significant improvement over operator image inspection in terms of accuracy for a single frame of videotape (assuming a great deal of time is allowed for visual inspection of image data).

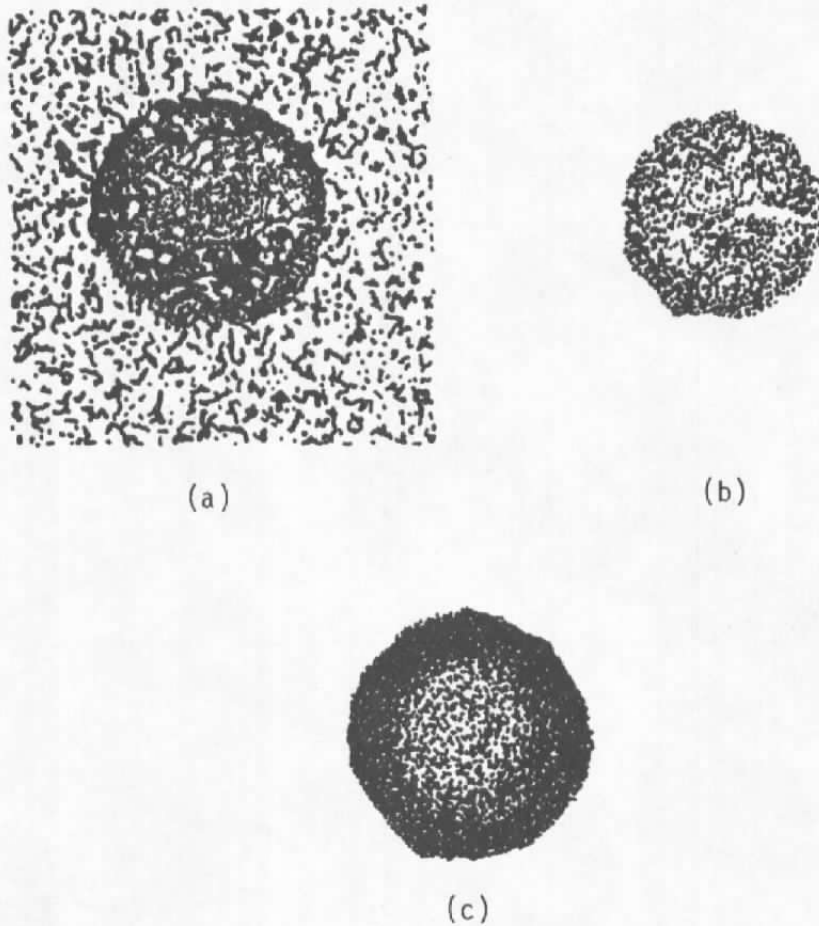
From the results of this study, the following recommendations are made:

1. The combined gradient and K-means techniques should be used to measure other objects (besides the throat simulator) with exactly known dimensions (this will further test the analysis techniques).
2. Experiments should be performed with image pre-processing (high-pass filtering and contrast stretching). Prior to measurement analysis, only image processing by frame averaging was performed because of limitations in image processor availability.
3. Consideration should be given to motor vibration during an actual firing. Can the prefire reference always be used as a standard unit of measure if the motor is shifting because of vibration?

4. These measurement techniques were designed to be a two-dimensional analysis. Since, for instance, rocket motor throat erosion will likely not be symmetric about the nozzle, a three-dimensional technique is preferred. Efforts to initiate three-dimensional image measurement capability should be based on the results previously presented.

## REFERENCES

1. Gonzalez, R. C. and Wintz, P. *Digital Image Processing*. Addison-Wesley, Reading, Massachusetts, 1977.
2. Davis, L. S., Rosenfeld, A. and Weszka, J. "Region Extraction by Averaging and Thresholding." *IEEE Transactions on Systems, Man, and Cybernetics*, May 1975, pp. 383-388.
3. Ballard, D. H. and Brown, C. M. *Computer Vision*. Prentice Hall, Englewoods Cliffs, New Jersey, 1982.
4. Tou, J. T. and Gonzalez, R. C. *Pattern Recognition Principles*. Addison-Wesley, Reading, Massachusetts, 1974.
5. Walker, R. Y., Gamble, R. A., and Smith, L. M. "In-Situ Solid-Propellant Burn-rate Measurements Using Flash Cineradiography." AEDC-TR-85-22 (AD-A167637), April 1986.



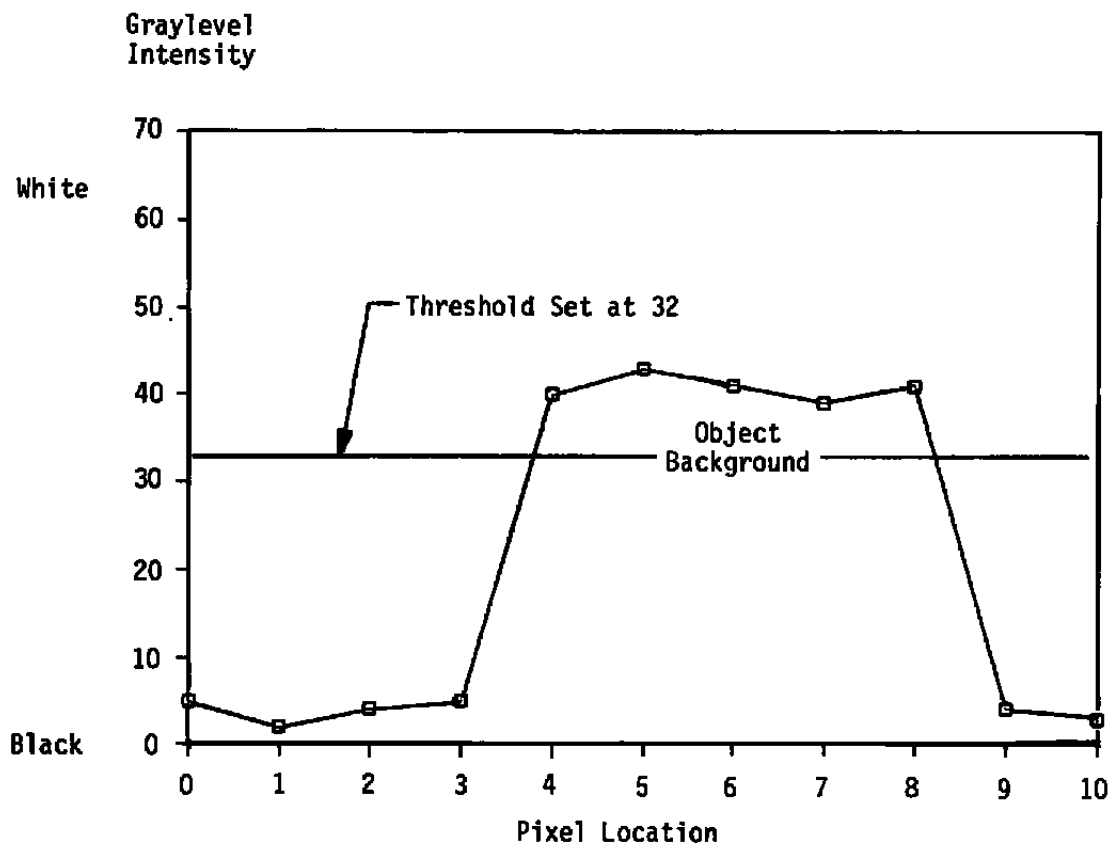
- Note: (a) Original black-and-white picture.  
(b) Result of locally averaging (a),  
using 11-by-11 neighborhood at  
each point.  
(c) Result of thresholding (b) at  
32 (on gray scale of 0 to 63).

**Figure 1. An example of averaging and thresholding.**



3	6	7	5	6	3	5
2	2	4	2	5	3	4
5	6	4	4	4	6	5
4	5	4	5	4	5	6
4	6	3	40	6	4	4
2	5	43	43	42	6	7
5	4	44	41	45	2	4
4	4	39	39	42	6	4
5	6	4	41	3	5	4
4	3	5	4	4	6	6
5	7	6	3	4	5	4

a. Digitized image of the moon



b. Profile of image column

Figure 2. Use of the threshold method.

0	1
-1	0

1	0
0	-1

**a. Roberts**

-1	0	1
-1	0	1
-1	0	1

1	1	1
0	0	0
-1	-1	-1

**b. Prewitt**

-1	0	1
-2	0	2
-1	0	1

1	2	1
0	0	0
-1	-2	-1

**c. Sobel****Figure 3. Different techniques for approximating the gradient of an image.**

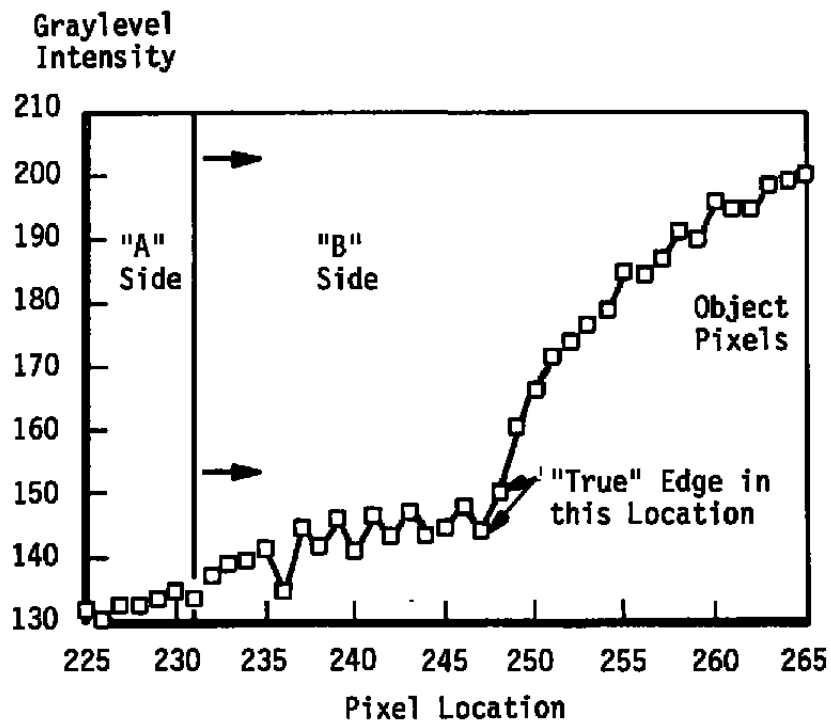
132	133	133	130	→	132
132	131	130	129	→	130.5
131	132	134	135		133
131	134	134	133		133
136	134	133	133		134
136	136	135	132		134.75
133	132	135	135		133.75
138	138	138	137		137.75
138	139	141	140		139.5
140	141	140	139		140
144	142	141	139		141.5
132	134	136	139		135.25
144	145	145	144		144.5
142	142	142	142		142
145	146	147	145		145.75
141	141	141	141		141
145	147	148	146		146.5
146	144	143	141		143.5
148	147	147	146		147
142	144	145	145		144
144	145	146	145		145
148	148	149	148		148.25
146	145	144	142		144.25
151	150	150	150		150.25
158	160	163	162		160.75
165	167	167	167		166.5
172	172	172	172		172
172	173	174	178		174.25
177	176	177	178		177
177	178	179	182		179
186	186	185	184		185.25
182	184	186	188		185
188	187	187	188		187.5
190	192	192	193		191.75
190	191	191	190		190.5
191	196	199	199		196.25
195	195	195	195		195
195	195	195	195		195
197	199	201	200		199.25
198	199	201	201		199.75
203	202	200	197		200.5

Note: If the edge is exactly in the 'row' direction, averaging will remove noise without degrading the image.

a. Digital image data

b. Data averaged

Figure 4. Use of the K-means algorithm.



c. Profile of averaged data  
Figure 4. Concluded.

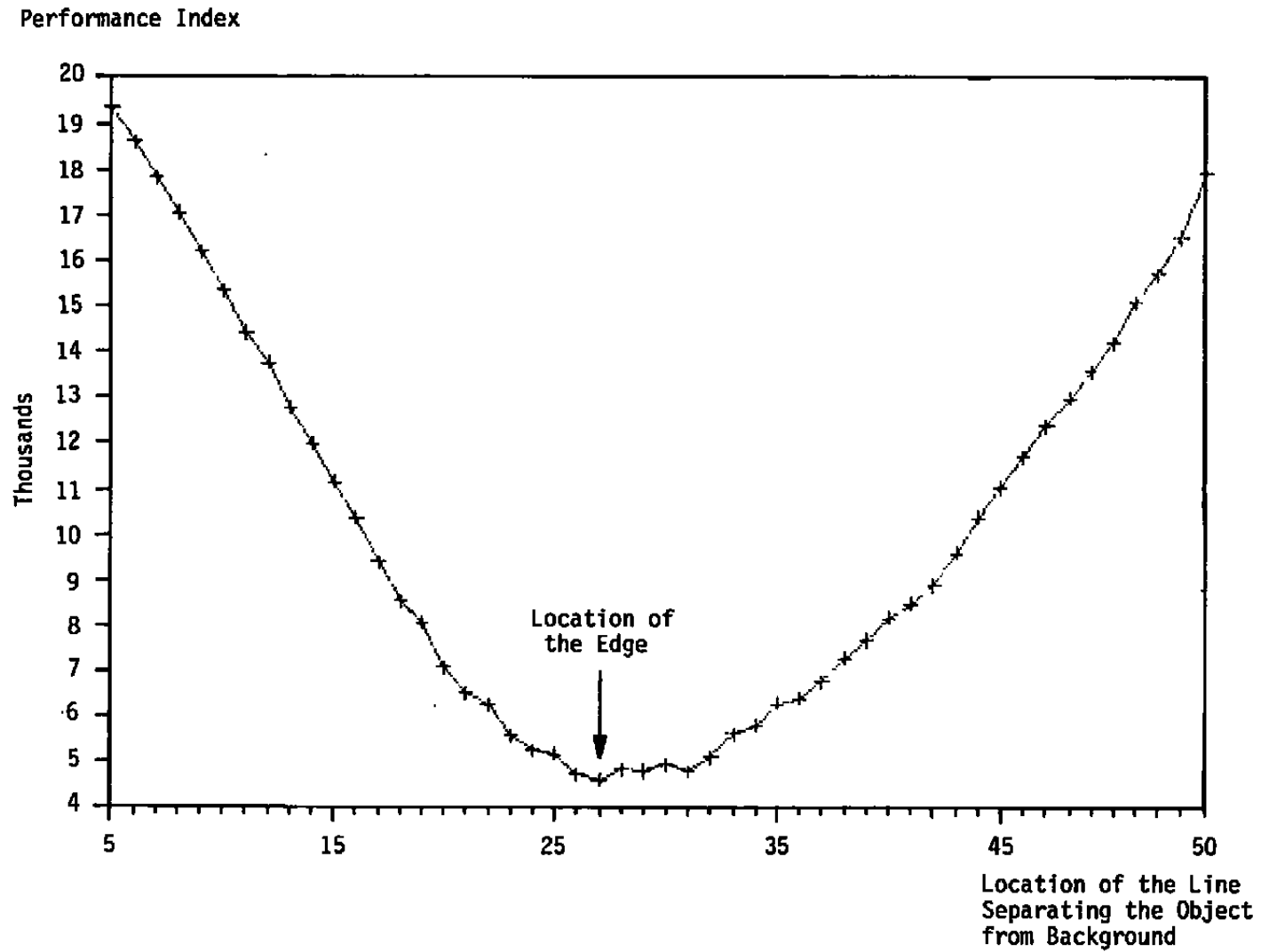
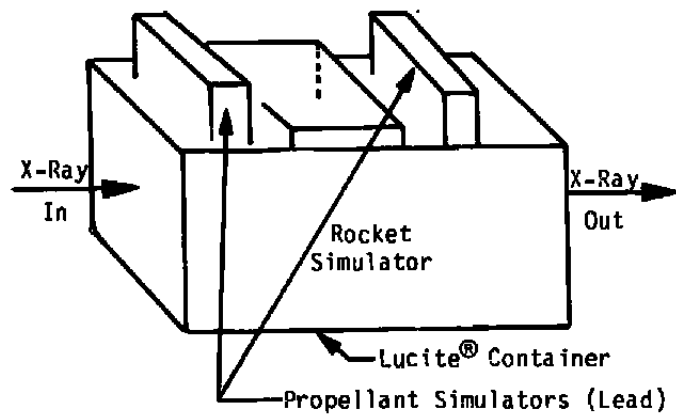
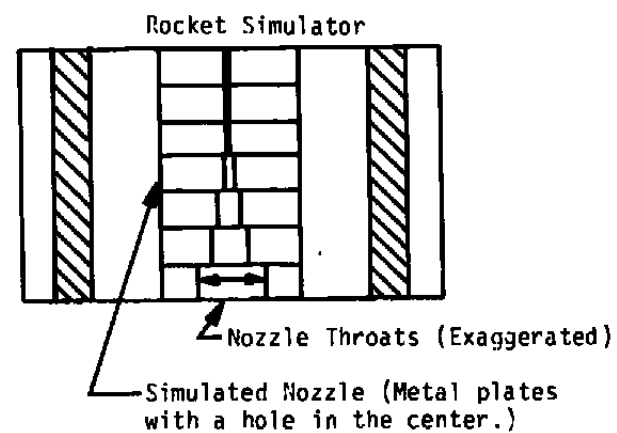


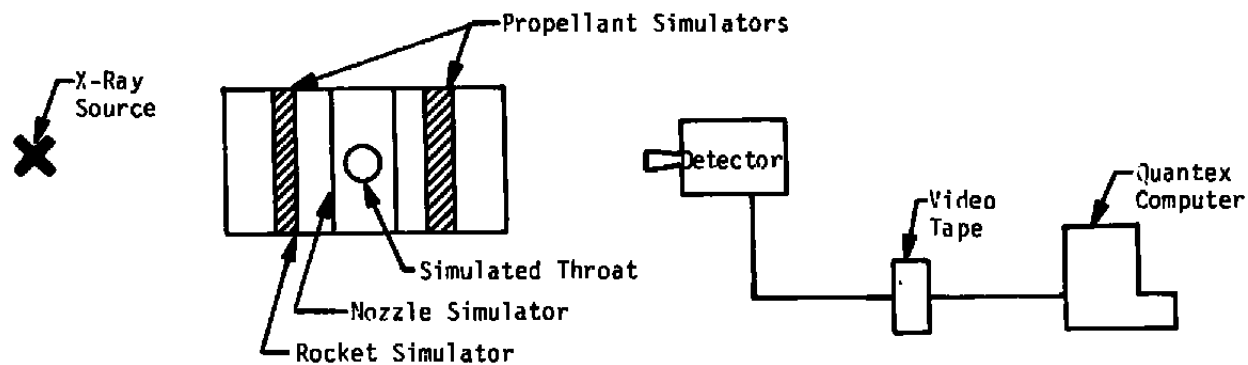
Figure 5. Typical profile for performance index.



**a. Overview**



**b. Top view**



**c. Side view**

**Figure 6. Overview of nozzle throat simulator.**

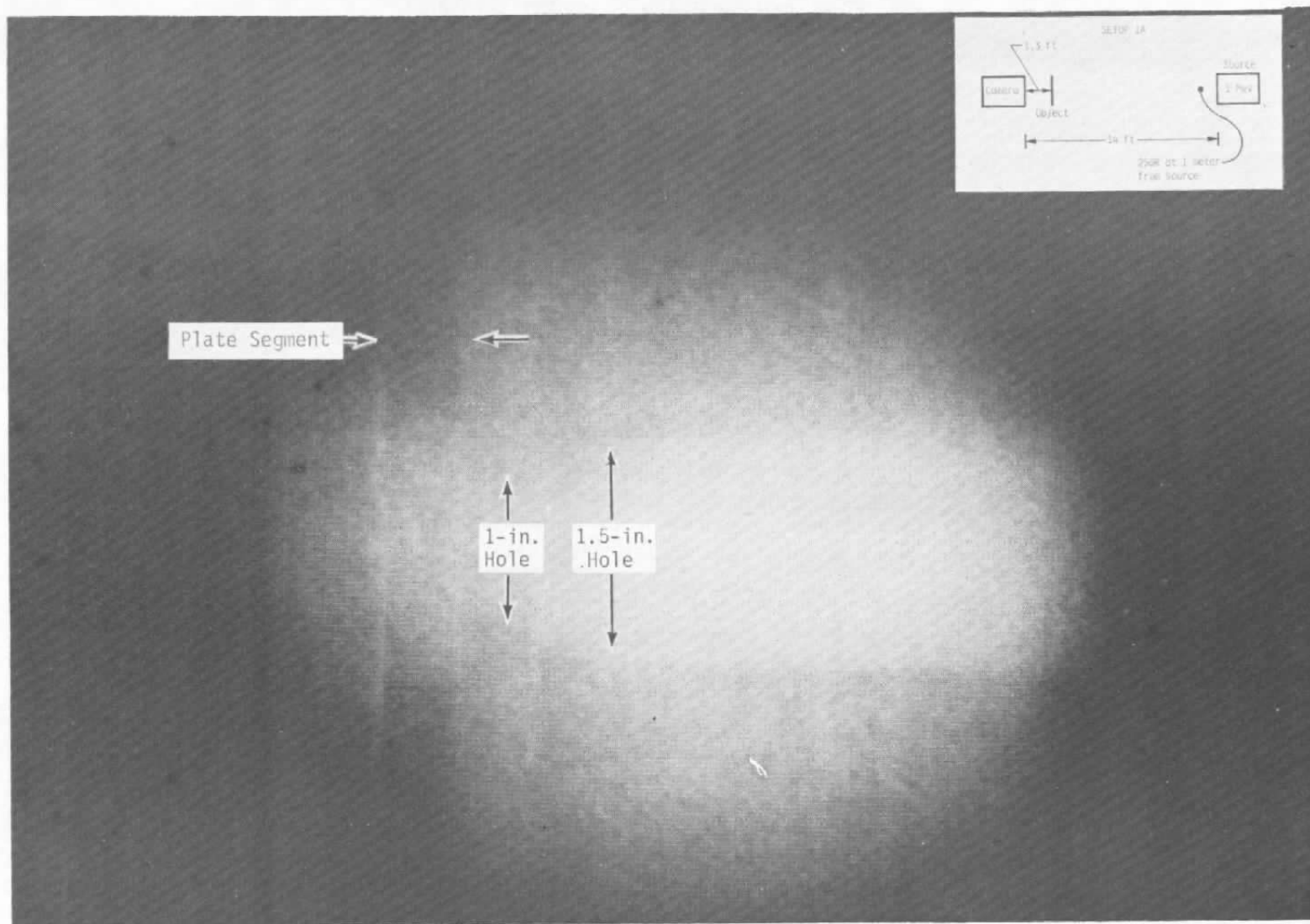


Figure 8. Computer image of simulator.

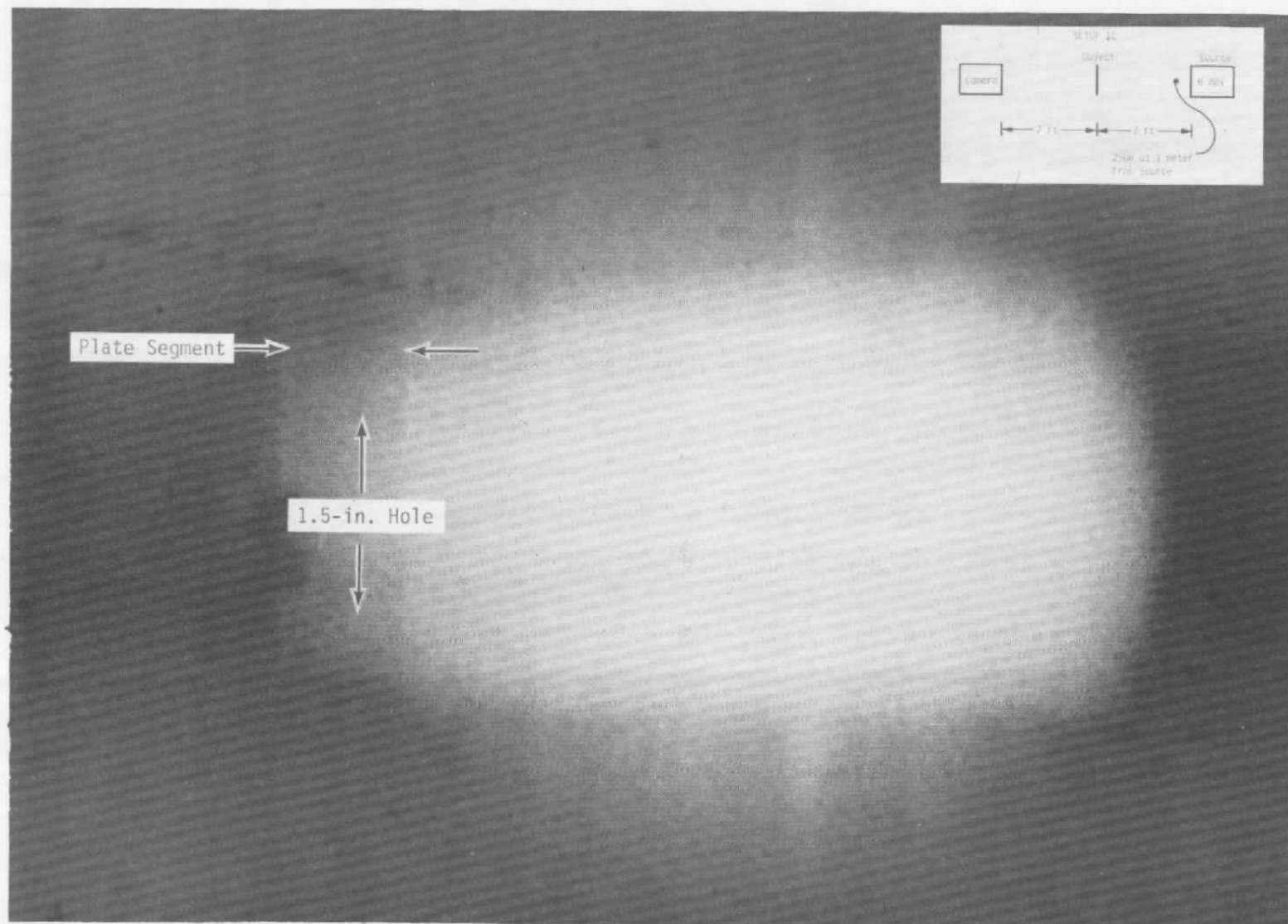
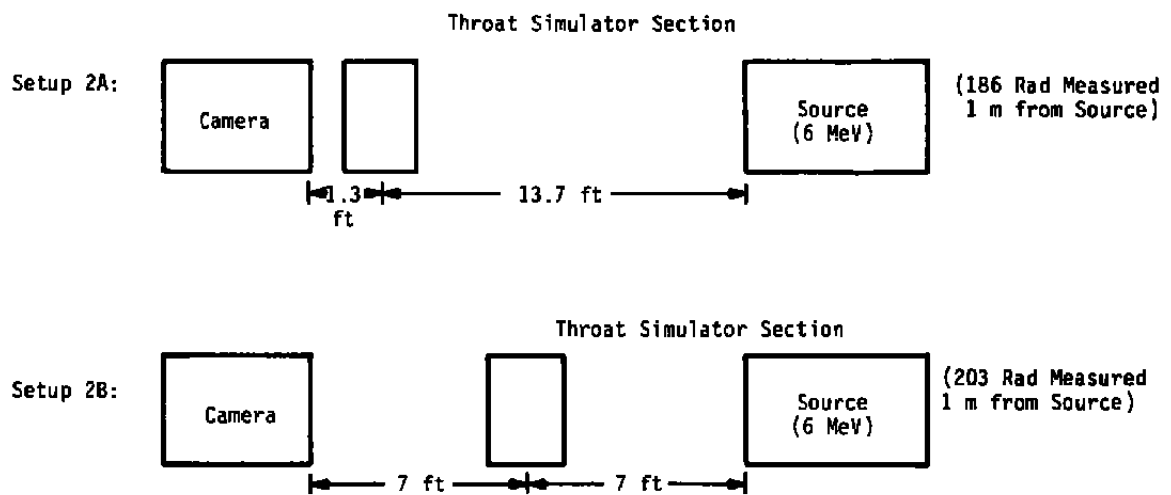
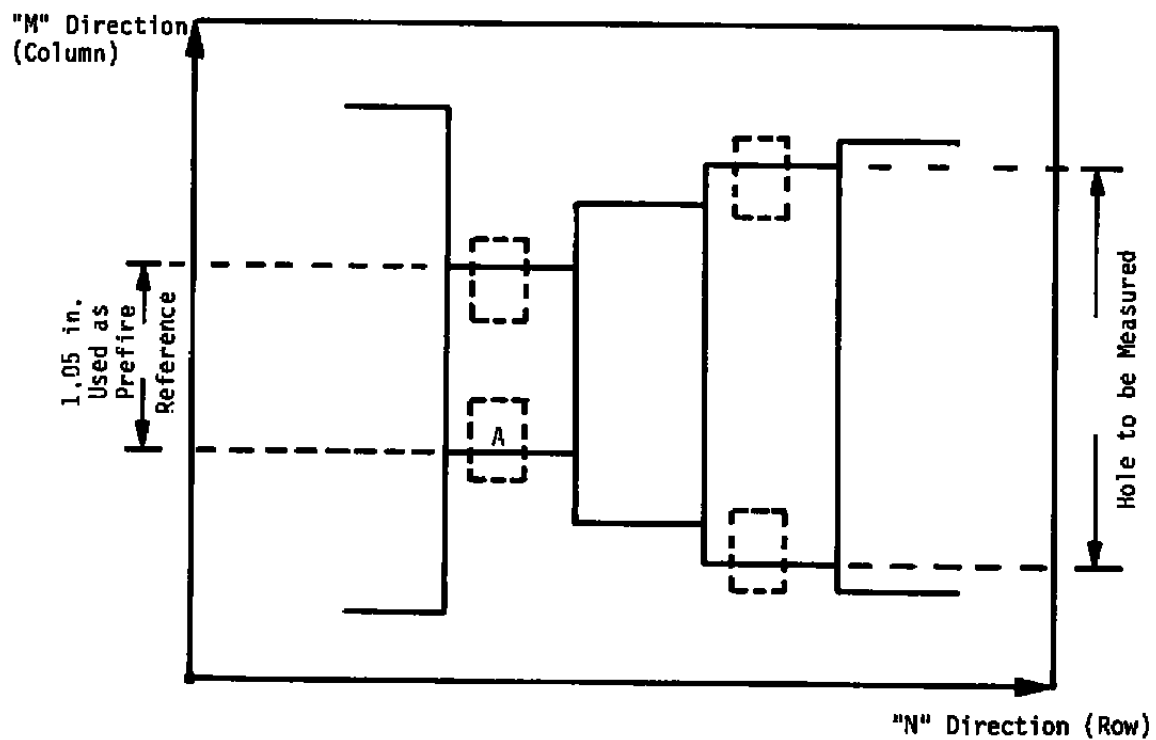


Figure 9. Object magnified by 100 percent.





**Figure 10. Data acquisition setup no. 2.**



a. Computer image of simulator

Figure 11. Example of an image area selection.

Image Data  
Area "A"  
(Fig. 11a)

132	133	133	130	→	132
132	131	130	129	→	130.5
131	132	134	135		133
131	134	134	133		133
136	134	133	133		134
136	136	135	132		134.75
133	132	135	135		133.75
138	138	138	137		137.75
138	139	141	140		139.5
140	141	140	139		140
144	142	141	139		141.5
132	134	136	139		135.25
144	145	145	144		144.5
142	142	142	142		142
145	146	147	145		145.75
141	141	141	141		141
145	147	148	146		146.5
146	144	143	141		143.5
148	147	147	146		147
142	144	145	145		144
144	145	146	145		145
148	148	149	148		148.25
146	145	144	142		144.25
151	150	150	150		150.25
158	160	163	162		160.75
165	167	167	167		166.5
172	172	172	172		172
172	173	174	178		174.25
177	176	177	178		177
177	178	179	182		179
186	186	185	184		185.25
182	184	186	188		185

Data  
Averaged

**b. Data from selected areas**

**Figure 11. Concluded.**

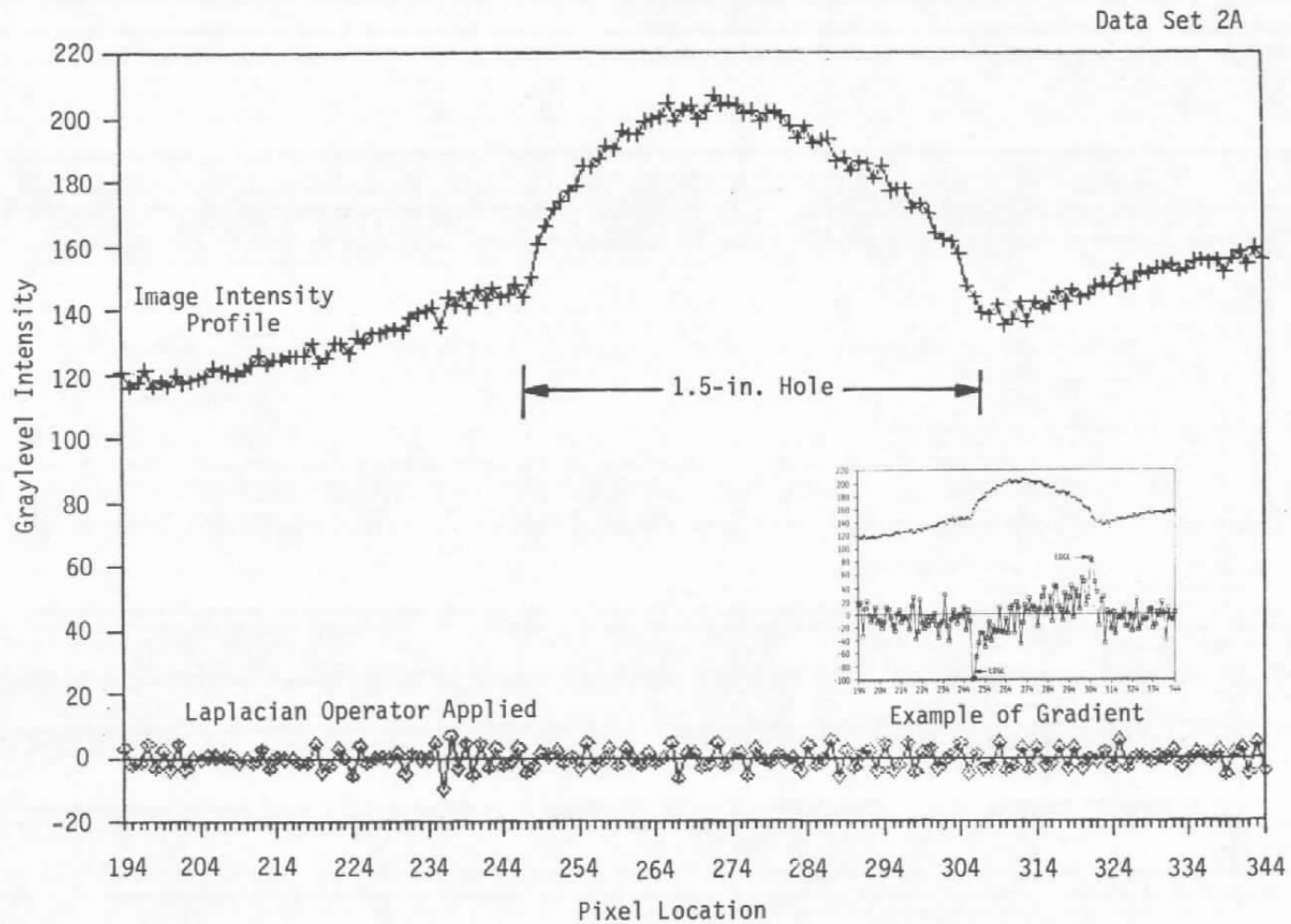
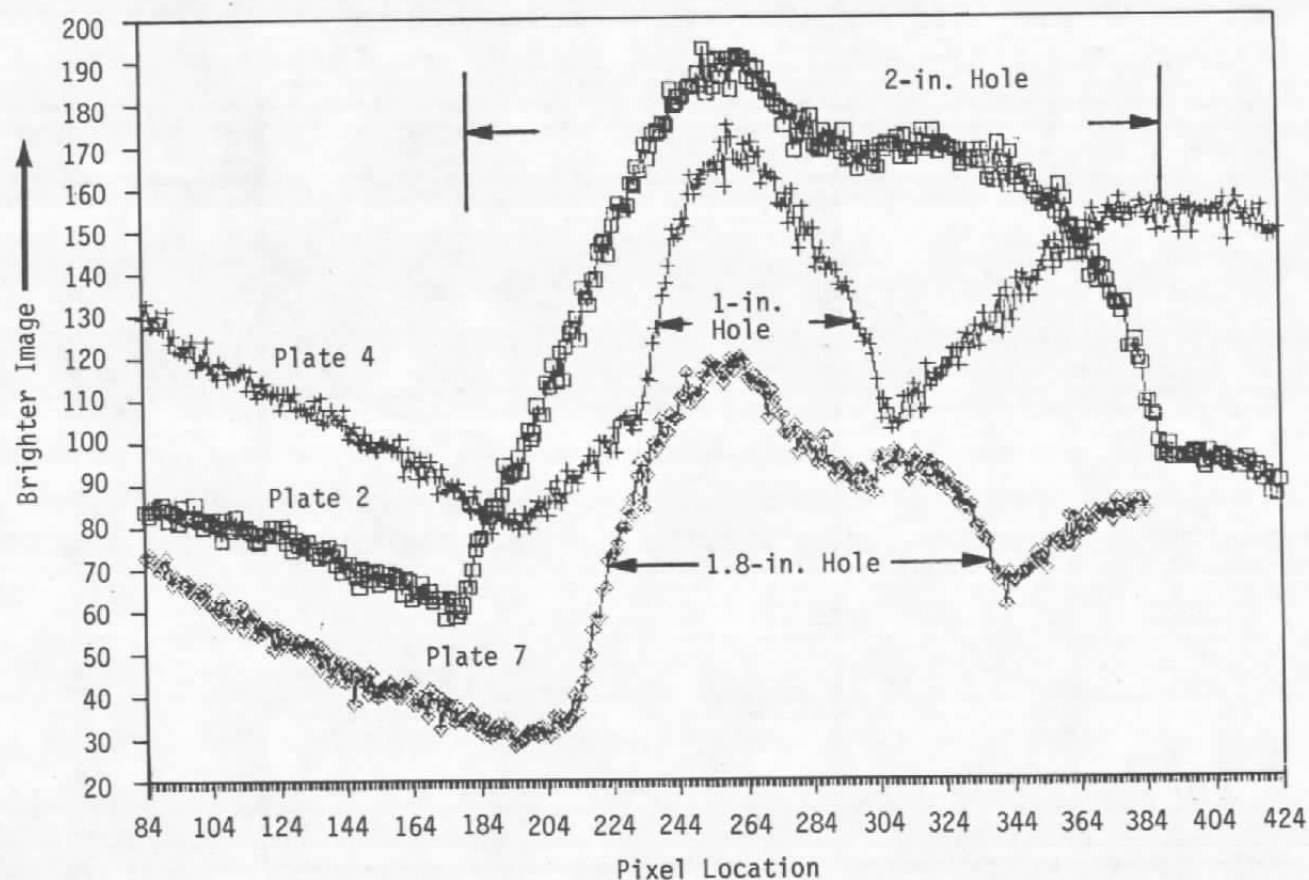


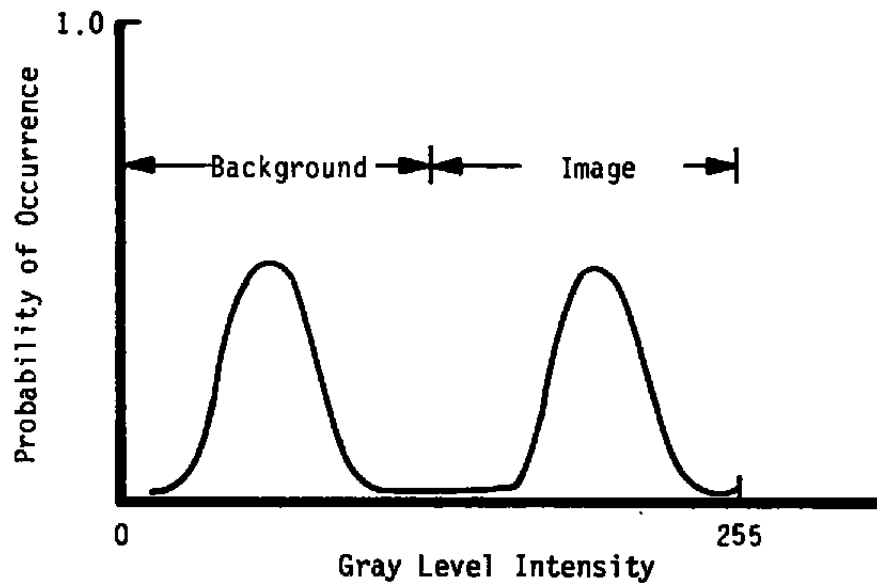
Figure 12. Example of Laplacian operator.

Graylevel Intensity

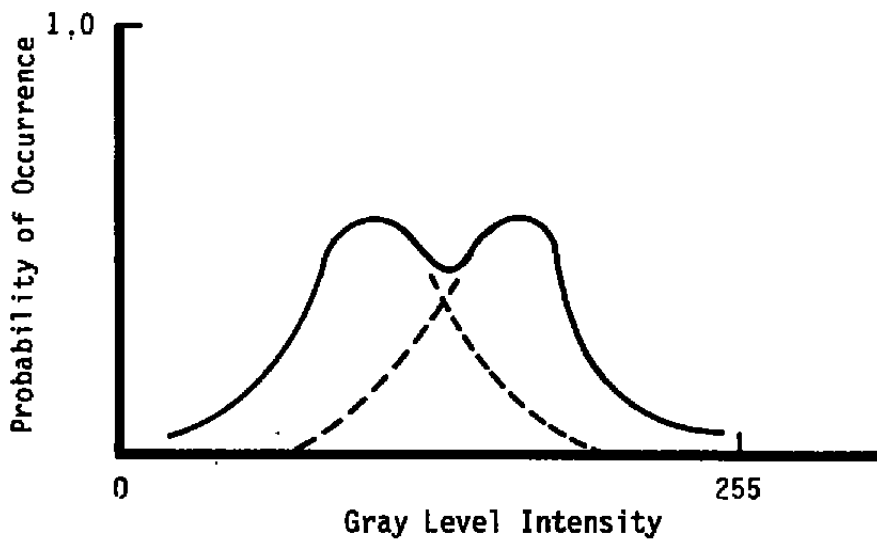


- Note:
1. Density constant in material surrounding hole (plate thickness constant) however, graylevel intensity varies.
  2. Graylevel intensity varies from plate to plate.
  3. Dark area (Plate 4) about the same graylevel intensity as light area (Plate 7).

**Figure 13. Variance in plate-to-plate graylevel intensity.**



**a. Desired**



**b. Actual**

**Figure 14. Throat simulator image histogram.**

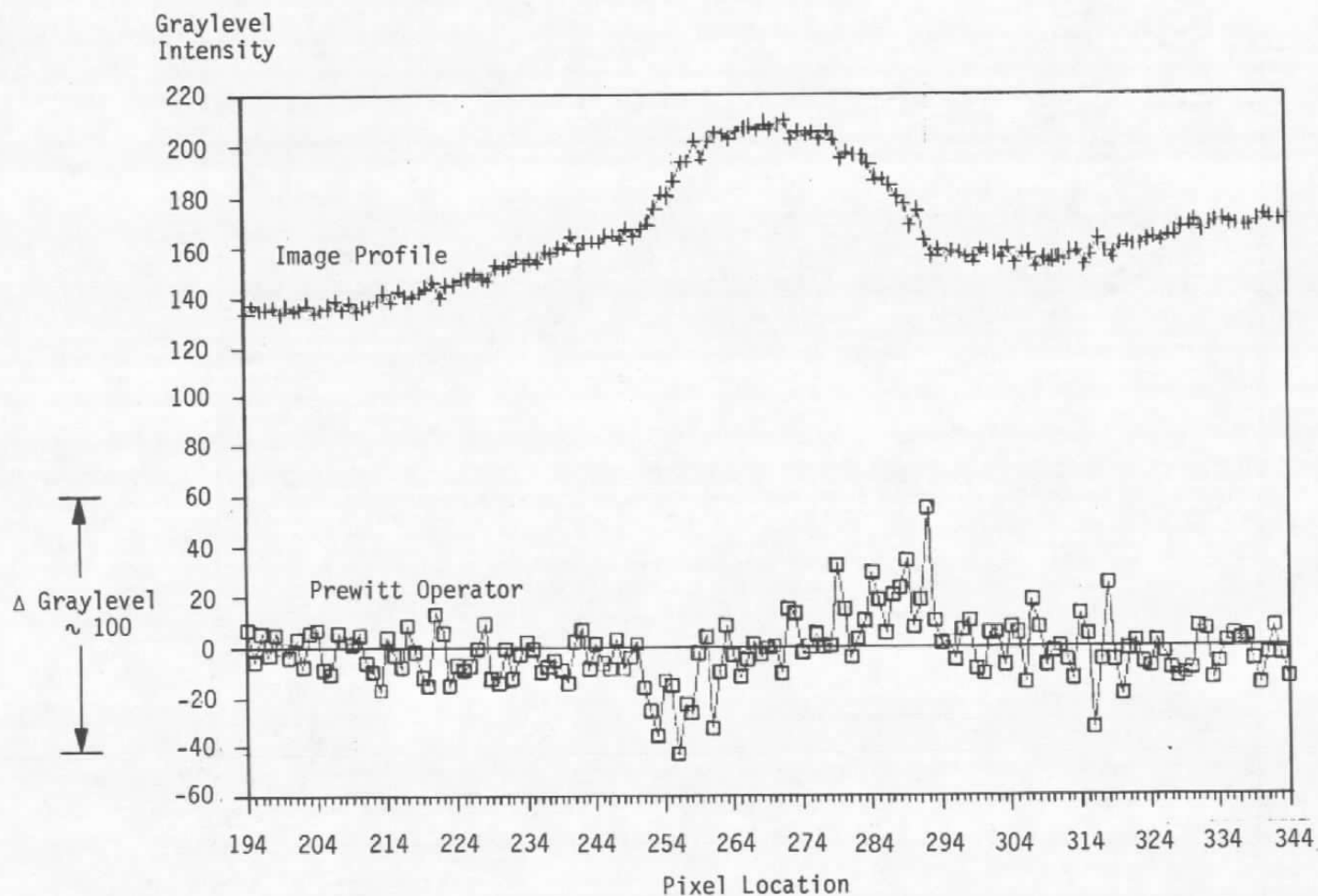


Figure 15. Application of Prewitt operator.

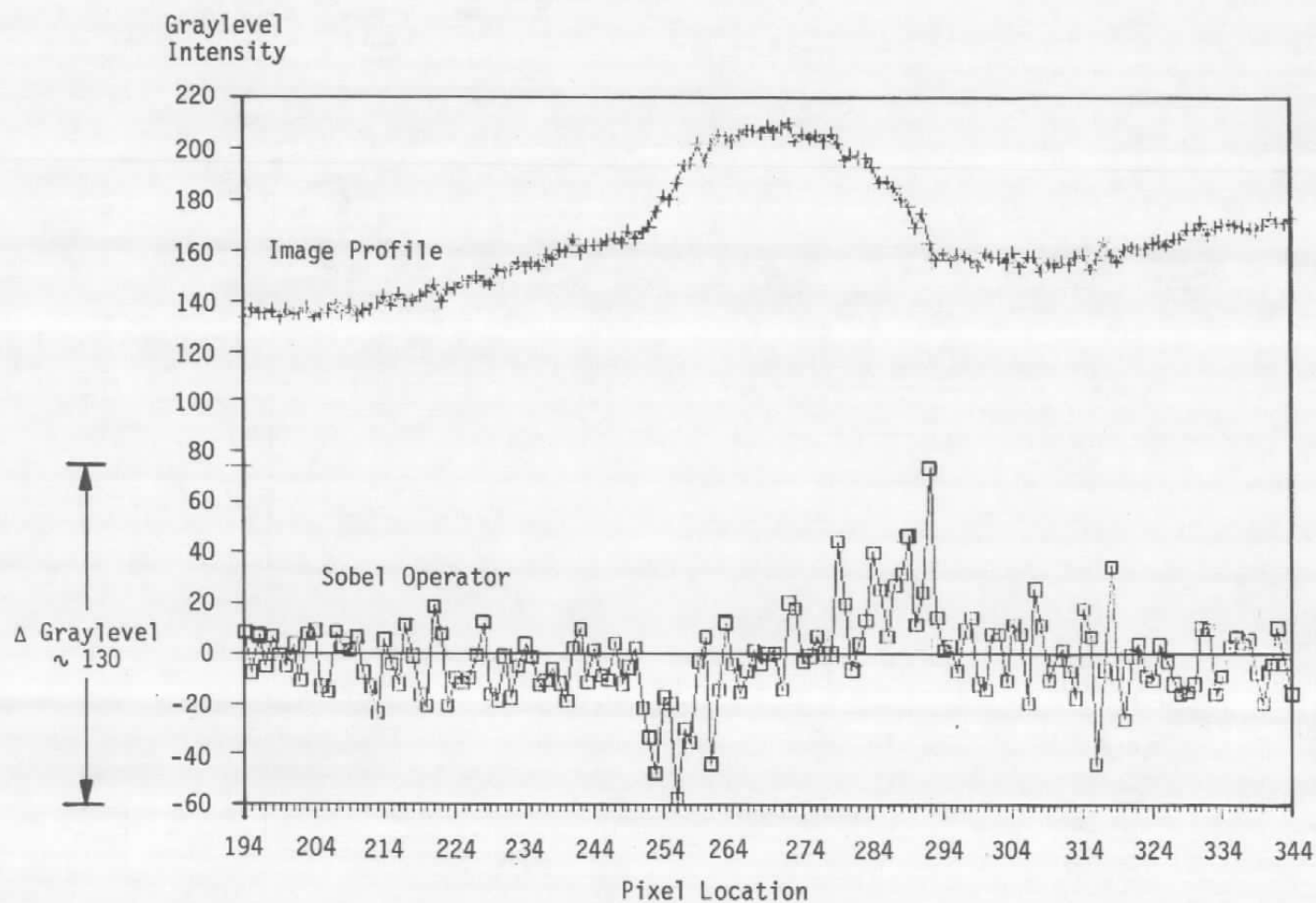


Figure 16. Application of Sobel operator.



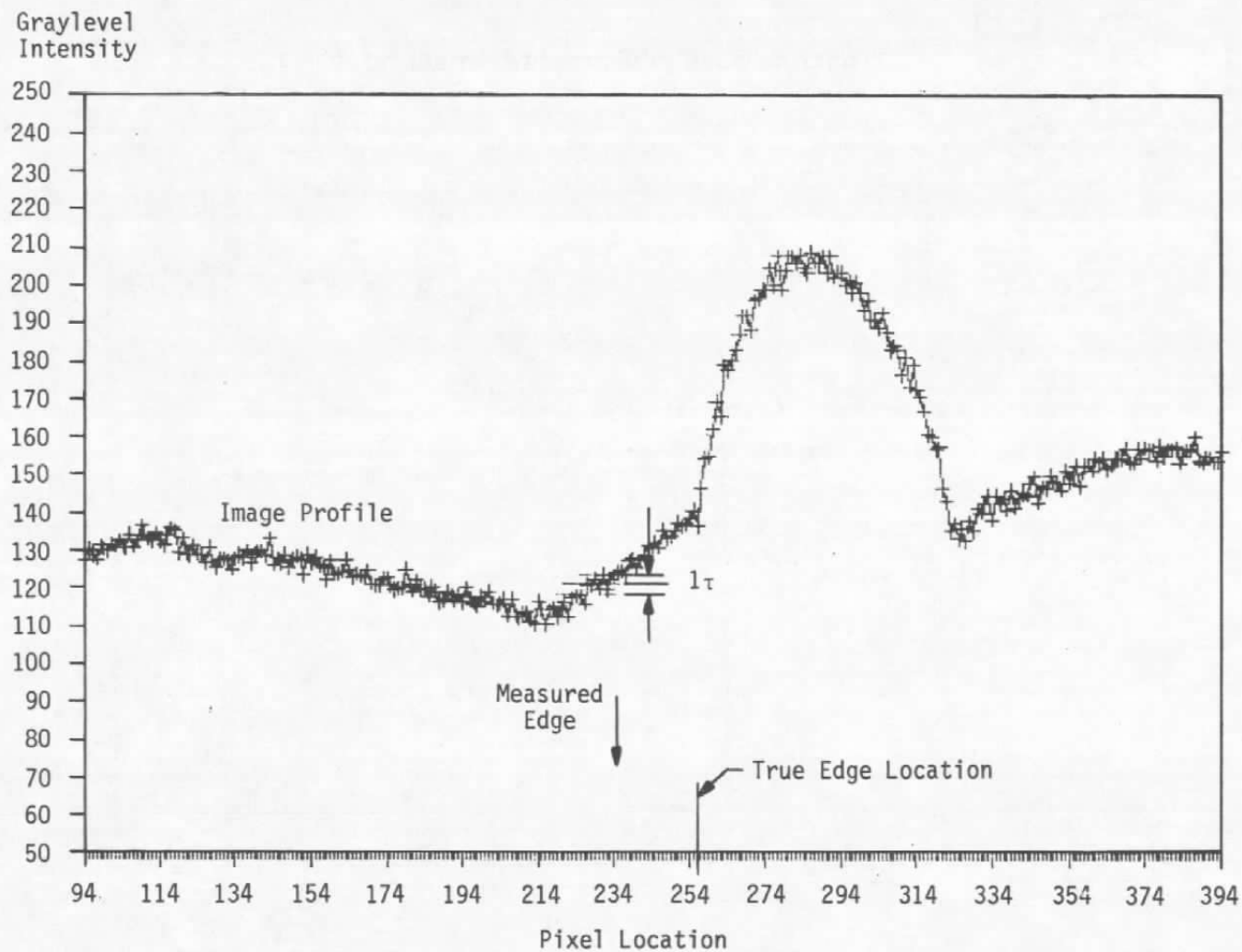


Figure 17. Problem with graylevel thresholding.

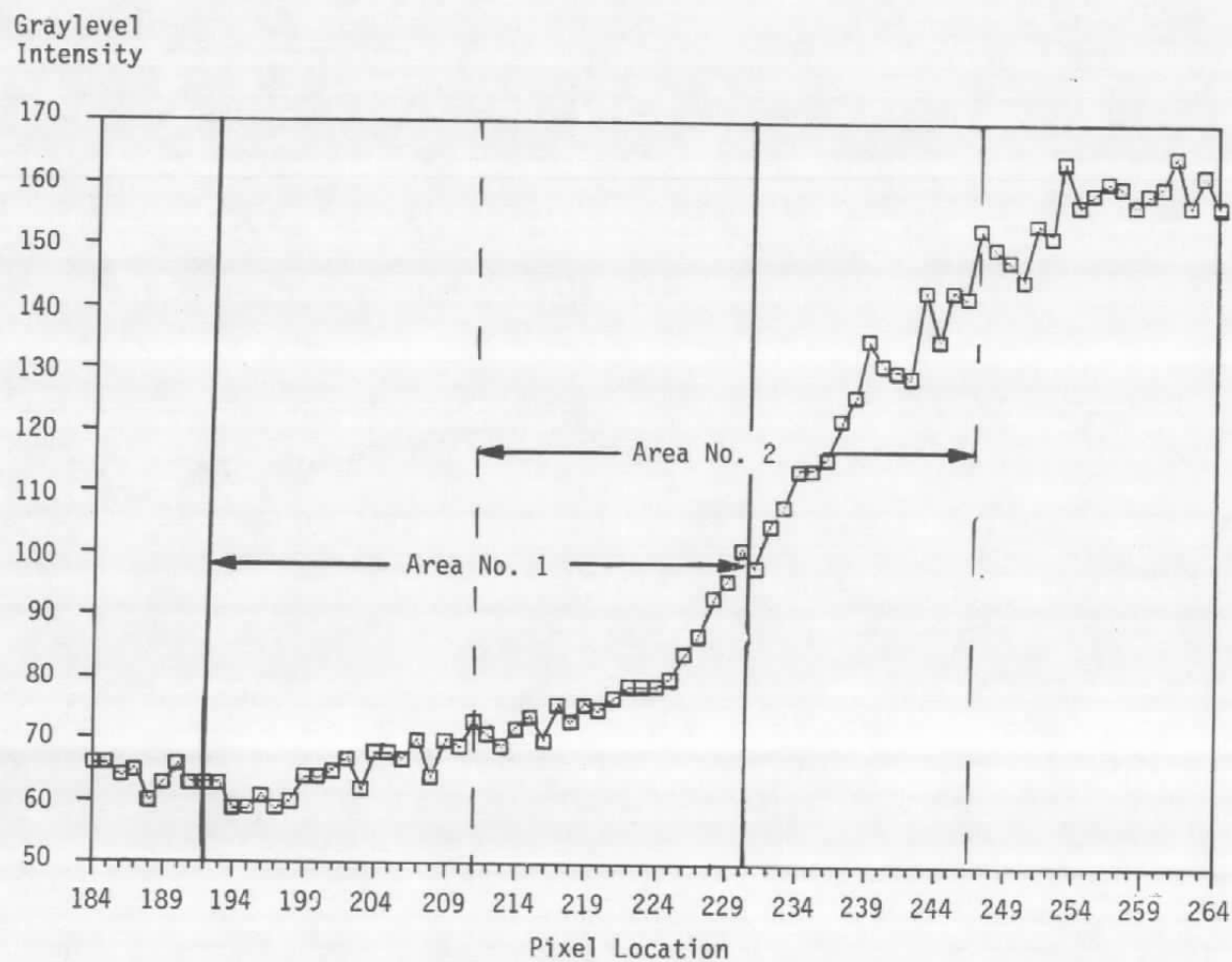


Figure 18. Influence of area selection on K-mean results.

**Table 1. Edge Detection Results on a Good Image**

Data Set 2A

Known Hole Size	Thresholding		Gradient (Sobel)		K-Means*	
	Computed Results	Error, percent	Computed Results	Error, percent	Computed Results	Error, percent
2.950 in.	~1.5 in.	~50	3.214 in.	+8.9	2.588 in.	-12.2
1.500 in.	~0.9 in.	~40	1.579 in.	+5.2	1.522 in.	+1.5
1.700 in.	---	---	1.804 in.	+5.8	1.649 in.	-3.0
1.808 in.	---	---	1.917 in.	+6.0	1.700 in.	-5.5

\* Results dependent on amount of data analyzed (in measuring the 2.950-in. hole, computed results ranged from 2.00 to 3.07 in., depending upon image data selected).

**Table 2. Edge Detection for Various Test Setups**

True Hole Size, in.	Data Set 2A			Data Set 2B	Data Set 1A	Data Sea 1A	Data Set 1C
	Gradient (Alone)	K-Means (Alone)	Combined	Combined (Magnified Object)	Combined Degraded Image)	Gradient Alone (Degraded Image)	Combined Magnified Object (Degraded Image)
2.950	3.214 (+ 8.9%)	2.588 (- 12.3%)	3.071 (+ 4.1%)	3.060 (+ 3.7%)	2.873 (- 2.6%)	3.276 (+ 11%)	*
1.500	1.579 (+ 5.3%)	1.522 (+ 1.5%)	1.560 (+ 4.0%)	1.373 (- 8.5%)	1.486 (- 1.4%)	(Not Measured)	1.439 (- 4.1%)
1.700	1.804 (+ 6.1%)	1.649 (- 3.0%)	1.718 (+ 1.1%)	1.702 (+ 0.1%)	1.838 (+ 8.1%)	2.050 (+ 21%)	1.614 (- 5.0%)
1.808	1.917 (+ 6.0%)	1.700 (- 6.0%)	1.848 (+ 2.2%)	1.851 (+ 2.4%)	1.720 (- 4.9%)	2.140 (+ 18%)	1.809 (0%)

\* Out of field of view after image magnification.

Note: ( ) indicates measurement error.

**Table 3. Computer vs. Visual Results**

True Hole Size, in.	Data Set 2A	
	Gradient and K-Means Combined	Results from Visual Inspection
2.950	3.071 (+ 4.1%)	2.948 (0%)
1.500	1.560 (+ 4.0%)	1.450 (- 3.3%)
1.700	1.718 (+ 1.1%)	1.619 (- 4.8%)
1.808	1.848 (+ 2.2%)	1.740 (- 3.8%)

Note: ( ) indicates measurement error.